Polaron-Driven Surface Reconstructions

Michele Reticcioli,[1] Martin Setvin,[2,*] Xianfeng Hao,[1,3] Peter Flauger,[1] Georg Kresse,[1] Michael Schmid,[2] Ulrike Diebold,[2] and Cesare Franchini[1,†]

[1]*University of Vienna, Faculty of Physics and Center for Computational Materials Science, A-1090 Vienna, Austria*

[2]*Institute of Applied Physics, Technische Universität Wien, A-1040 Vienna, Austria*

[3]*Key Laboratory of Applied Chemistry, Yanshan University, Qinhuangdao 066004, People's Republic of China*

(Received 24 May 2017; revised manuscript received 7 July 2017; published 25 September 2017)

Geometric and electronic surface reconstructions determine the physical and chemical properties of surfaces and, consequently, their functionality in applications. The reconstruction of a surface minimizes its surface free energy in otherwise thermodynamically unstable situations, typically caused by dangling bonds, lattice stress, or a divergent surface potential, and it is achieved by a cooperative modification of the atomic and electronic structure. Here, we combined first-principles calculations and surface techniques (scanning tunneling microscopy, non-contact atomic force microscopy, scanning tunneling spectroscopy) to report that the repulsion between negatively charged polaronic quasiparticles, formed by the interaction between excess electrons and the lattice phonon field, plays a key role in surface reconstructions. As a paradigmatic example, we explain the (1×1) to (1×2) transition in rutile $TiO_2(110)$.

DOI: 10.1103/PhysRevX.7.031053

Subject Areas: Condensed Matter Physics, Physical Chemistry, Semiconductor Physics

I. INTRODUCTION

The majority of surfaces undergo significant structural and electronic modifications with respect to the ideal bulk phase in order to minimize their surface free energy [1]. Typical mechanisms reduce the number of surface dangling bonds, compensate intrinsic polarity, or decrease the lattice stress [1–4]. Prototypical examples are the $Si(111)$-(7×7) reconstruction [5,6], the $(n \times 1)$ and $(2 \times n)$ reconstructions occurring on the $SrTiO_3(110)$ surface [7,8], and the (110) missing-row or (100)-hexagonal structures observed on the fcc metals Au, Pt, and Ir [9–11], respectively.

Unraveling the physical mechanism that drives such surface reconstructions is essential to understand physical and chemical properties of surfaces, and it helps optimize materials performance in applications such as microelectronics, catalysis, fuel cells, or surface engineering. The stabilization process typically involves the displacements of surface atoms and electric charge transfer between surface atoms, and often results in nonstoichiometric reconstructions; this mechanism can be affected by defects and heating treatments, and by the interaction of orbitals, lattice, and spins [1,12]. In this work, we find that charge trapping can cause surface reconstructions as well.

Excess charge in a flexible and ionic lattice is often present in the form of small polarons, i.e., trapped electrons or holes coupled with the lattice phonon field. Manifestations include a local alteration of the bond lengths, a change of the formal valence at the specific polaronic site, and the emergence of a characteristic peak well localized in the gap region [13–17]. Polarons play a decisive role in electron transport, optical absorption, and chemical reactivity, and have crucial implications in other diverse phenomena including high-T_c superconductivity [18], colossal magnetoresistance [19,20], thermoelectricity [21], and photochemistry [22]. Formation of polarons is particularly favorable in transition-metal oxides, owing to the strength of the electron-phonon interaction, and is further promoted in the vicinity of a surface, where the crystal lattice is more flexible and the necessary lattice relaxations cost less energy [23–25].

Titanium dioxide, TiO_2, is an archetypal polaron system. The surfaces of this material have been studied extensively in both theory and experiment [24,26,27]. TiO_2 single crystals are often reduced, either chemically (by removing O from the lattice, i.e., by creating an oxygen vacancy V_O) or electronically (by adding excess electrons through the introduction of extrinsic dopants). This reduction produces polarons that typically reside in subsurface Ti^{3+} sites, although hopping can be thermally activated [17,24].

*setvin@iap.tuwien.ac.at

†cesare.franchini@univie.ac.at

For highly reduced rutile $TiO_2(110)$ samples, the surface assumes a (1×2) reconstruction rather than a (1×1) termination that is observed on more stoichiometric crystals [4,28,29]. This (1×2) structure is then the low-temperature phase; it can reversibly switch to the (1×1) phase when the sample temperature is raised above approximately 1000 K [30], and the transition is facilitated by the surface-to-bulk mass flow [31]. Here, we evaluate the surface structure as a function of oxygen vacancy concentration (at the surface), c_{V_O}, using density functional theory (DFT), first-principles molecular dynamics (FPMD), scanning tunneling microscopy (STM), and atomic force microscopy (AFM). We find that, with increasing V_O density, the resulting polarons tend to form an optimum 3×1 arrangement in the (1×1) surface. When c_{V_O} is further raised, the repulsive interaction between these negatively charged quasiparticles increases the surface free energy. The resulting energy instability is overtaken by the geometrical reconstruction into the (1×2) phase.

II. METHODS

A. *Ab initio* calculations

We used DFT and FPMD to investigate the (1×1) and (1×2) surface phases of the $TiO_2(110)$ rutile. The calculations were performed using the Vienna *ab initio* simulation package (VASP) [32,33]. We adopted the generalized gradient approximation (GGA) within the Perdew, Burke, and Ernzerhof parametrization [34], with the inclusion of an on-site effective U of 3.9 eV on Ti d-states. In our previous work [17], we calculated this value within the constrained random phase approximation (cRPA) [35] and confirmed that it correctly predicts the experimentally observed degree of localization in the TiO_2 polymorphs rutile and anatase. We also checked the robustness of our conclusions against other values of U (see Ref. [36]). The rutile $TiO_2(110)$ surfaces were modeled with an asymmetric slab containing five Ti layers with a large two-dimensional (2D) 9×2 unit cell, resulting in more than 500 atoms. The bottom two layers were kept fixed, whereas all the other atomic sites were relaxed using standard convergence criteria with a plane-wave energy cutoff of 300 eV (lowered to 250 eV for the FPMD runs) and using the Γ point only for the integration in the reciprocal space. For the (1×1) phase, up to nine oxygen vacancies (V_O's) were homogeneously included in the top layer (S0) at different concentrations ($c_{V_O} = 5.6\%$, 11.1%, 16.7%, 22.2%, 33.3%, 38.9%, 50.0%). This V_O distribution was chosen by taking into account the experimentally determined, spatially resolved, autocorrelation functions. More details on this choice are provided in Ref. [36]. Each V_O supplies two excess electrons, which form two polarons. The (1×2) phase was constructed according to the Ti_2O_3 model [4,37,38] by placing the reconstructed row on top of the five layers, which gives rise to two polarons per (1×2) unit cell.

The stability of the surface, and the thermally activated hopping behavior of the polarons, were inspected by combining FPMD at $T = 700$ K and static $T = 0$ K DFT calculations using the following strategy: First, for each phase and each c_{V_O}, multiple series of FPMD runs were conducted, each starting from an arbitrary polaronic configuration and lasting 10 ps with a time step of 1 fs. This leads to 10 000 different high-temperature structures for each FPMD run. Second, we selected all inequivalent polaronic configurations from this set; about 200 for each phase and V_O concentration. Finally, we relaxed these at $T = 0$ K and found the energetically most stable structure by comparing the total DFT energies. This procedure was repeated for the nine different V_O concentrations and for the Ti_2O_3 reconstructed model, by using the 9×2 cell. A slightly lower ground-state energy for the $c_{V_O} = 16.7\%$ case was obtained by adopting a 6×2 unit cell, which allows for a more homogeneous distribution of oxygen vacancies as compared to the 9×2 cell at this particular c_{V_O}. The charge densities of polarons in the most stable configurations were used for simulating STM images within the Tersoff-Hamann approach [39]. The resulting isosurface representations allow for comparison with our experimental data.

The total energies of the most stable configurations were used to build a global surface phase diagram using standard *ab initio* atomistic thermodynamics [40]. By neglecting configurational entropy and phonon contributions, the surface free energy ΔG can be approximated as follows:

$$\Delta G = \frac{1}{A}[E^{\mathrm{loc}} - n_{\mathrm{Ti}} E^{\mathrm{bulk}}_{\mathrm{TiO_2}} + \mu_{\mathrm{O}}(2n_{\mathrm{Ti}} - n_{\mathrm{O}})], \qquad (1)$$

where E^{loc} is the DFT total energy at $T = 0$ K for the surface slab with trapped polarons, and $E^{\mathrm{bulk}}_{\mathrm{TiO_2}}$ is the energy for the TiO_2 bulk. The adimensional prefactor $1/A$ scales the energy to the (1×1) surface cell. The weighted difference between the number of Ti (n_{Ti}) and O (n_{O}) atoms accounts for the deviation from the stoichiometric formula. The chemical potential μ_{O} of oxygen atoms was considered in terms of its deviation $\Delta\mu_{\mathrm{O}}$ from the total energy $E_{\mathrm{O_2}}$ of an isolated oxygen molecule:

$$\mu_{\mathrm{O}} = \left(\frac{1}{2}E_{\mathrm{O_2}} + \Delta\mu_{\mathrm{O}}\right). \qquad (2)$$

We also constructed an additional phase diagram describing the stability of $TiO_2(110)$ surfaces forced to have all the electrons delocalized. The delocalized solution was achieved by performing non-spin-polarized calculations. The surface free energy for the systems with all electrons delocalized is given by replacing the E^{loc} term in Eq. (1) with

the so-obtained, delocalized, ground-state energy $E^{\mathrm{deloc}}_{\mathrm{relax}}$, where the atoms were allowed to relax again.

Moreover, the most stable configurations were analyzed in terms of the polaron formation energy E_{POL}. E_{POL} represents the convenience for the system to trap electrons, and it is calculated as

$$E_{\mathrm{POL}} = E^{\mathrm{loc}} - E^{\mathrm{deloc}}_{\mathrm{relax}}. \quad (3)$$

The stability of a polaron, quantified by E_{POL}, is the result of the competition between the structural cost needed to distort the lattice in order to accommodate polarons (E_{ST}) and the electronic energy gained by localizing the electron in the distorted lattice (E_{EL}):

$$E_{\mathrm{POL}} = E_{\mathrm{EL}} + E_{\mathrm{ST}} \quad (4)$$

where E_{ST} is defined as

$$E_{\mathrm{ST}} = E^{\mathrm{deloc}}_{\mathrm{constr}} - E^{\mathrm{deloc}}_{\mathrm{relax}} \quad (5)$$

where $E^{\mathrm{deloc}}_{\mathrm{constr}}$ is the energy of the system forced to have only delocalized electrons and constrained into the structure of the system hosting polarons.

Finally, the results of the FPMD runs were also used to perform a statistical analysis of the polarons and their hopping behavior. For each phase and c_{V_O}, we determined the number of occurrences of charge trapping in each layer. We computed the polaron-polaron correlation function, defined as the distribution of the distance between two polarons at a given time step, averaged over all FPMD steps.

B. Experiments

Combined STM/AFM measurements were performed at $T = 78$ K in an ultrahigh vacuum (UHV) chamber with a base pressure below 2×10^{-9} Pa, equipped with a commercial Omicron q-Plus LT head. Synthetic single crystal samples (Crystec) were cleaned in an adjoining preparation chamber by repeated sputtering with 1 keV Ar^+ ions and annealing to 1000 K. All data were measured on a sample that was strongly reduced by more than 100 cycles of prior sputtering and annealing. Tuning-fork-based AFM sensors with a separate wire for the tunneling current were used ($k = 3750$ N/m, $f_0 = 47\,500$ Hz, $Q \approx 50\,000$) [41]. Glued to each tuning fork was an electrochemically etched W tip, which was cleaned *in situ* by field emission and self-sputtering in 10^{-4} Pa argon [42]. The tips were purposely functionalized by an O adatom. Here, the rutile surface was exposed to O_2, and bias pulses applied above adsorbed O_2 molecules occasionally resulted in a single O atom being picked up. Comparing force-distance curves (see Ref. [36]) measured above the clean (1×1) surface to previous experimental AFM works [43,44] leads us to conclude that the tip is terminated by a single-coordinated O atom (O adatom). In our experience, this is the only tip model where the attractive force above the highest O atoms (O_{2c}) is negligible and the repulsive regime is entered directly. With CO-functionalized tips [45], the same AFM contrast was obtained above the (1×2) reconstruction, but no good images were obtained on the (1×1) phase.

III. RESULTS

The transition from a (1×1) to a (1×2) structure at the rutile $TiO_2(110)$ surface is well documented in the literature [4,28]. The large-area STM image in Fig. 1 shows a surface typical for a strongly reduced $TiO_2(110)$ sample. The bulk-terminated (1×1) structure with isolated oxygen vacancies (V_O's) coexists with stripes of the (1×2) reconstruction. When a pristine (stoichiometric) TiO_2 sample is introduced into UHV, it shows only the (1×1) surface. The standard sample treatments described above, i.e., sputtering and high-temperature annealing, reduce the crystals and, at first, result in the appearance of isolated surface V_O's at the 2-fold coordinated oxygen (O_{2c}) sites. Eventually, the (1×2) stripes shown in Fig. 1(a) appear; their density increases upon further reduction until they cover the whole surface [28]. Here, we have only isolated (1×2) stripes [not a full (1×2) superstructure, which would be detectable by diffraction techniques].

This phase separation into (1×1) and (1×2) regions allows an accurate determination of the critical concentration of V_O's where the transition occurs. In the samples considered here, it is measured as a $16.7 \pm 0.2\%$ ($\approx 1/6$) monolayer.

A zoom-in of the (1×1) phase and a detail of the (1×2) reconstruction are shown in Figs. 1(f)–1(h) and Figs. 1(i)–1(k), respectively. Using an nc-AFM with an O tip termination allows us to image the O sublattice. On the well-known (1×1) phase [Fig. 1(f)], the image shows the O_{2c} atoms in the regime of repulsive forces; V_O's appear as missing spots in the rows. This imaging mode is particularly valuable on the (1×2) reconstruction [Fig. 1(i)], where the structural model is still under debate [4,37,38,47–50]. AFM allows a precise measurement of the positions of the surface O atoms in the x-y plane, which helps us exclude most of the proposed structures. Our results confirm the Ti_2O_3 model [Fig. 1(c)] initially proposed by Onishi and Iwasawa [4], recently refined by Wang *et al.* [37] via DFT-based genetic algorithms, and supported by total-reflection high-energy positron diffraction studies [38]. Here, the stripes have a Ti_2O_3 stoichiometry; i.e., their composition can be viewed as Ti_2O_4 with 50% of V_O's. The atom labeling for the (1×1) and (1×2) phases used in the discussion is specified graphically in Figs. 1(b) and 1(c).

While STM images [Figs. 1(g), 1(h), 1(j), and 1(k)] provide supplementary information about the geometric structure, their importance resides in unraveling the electronic structure of the two phases. In the empty-states STM

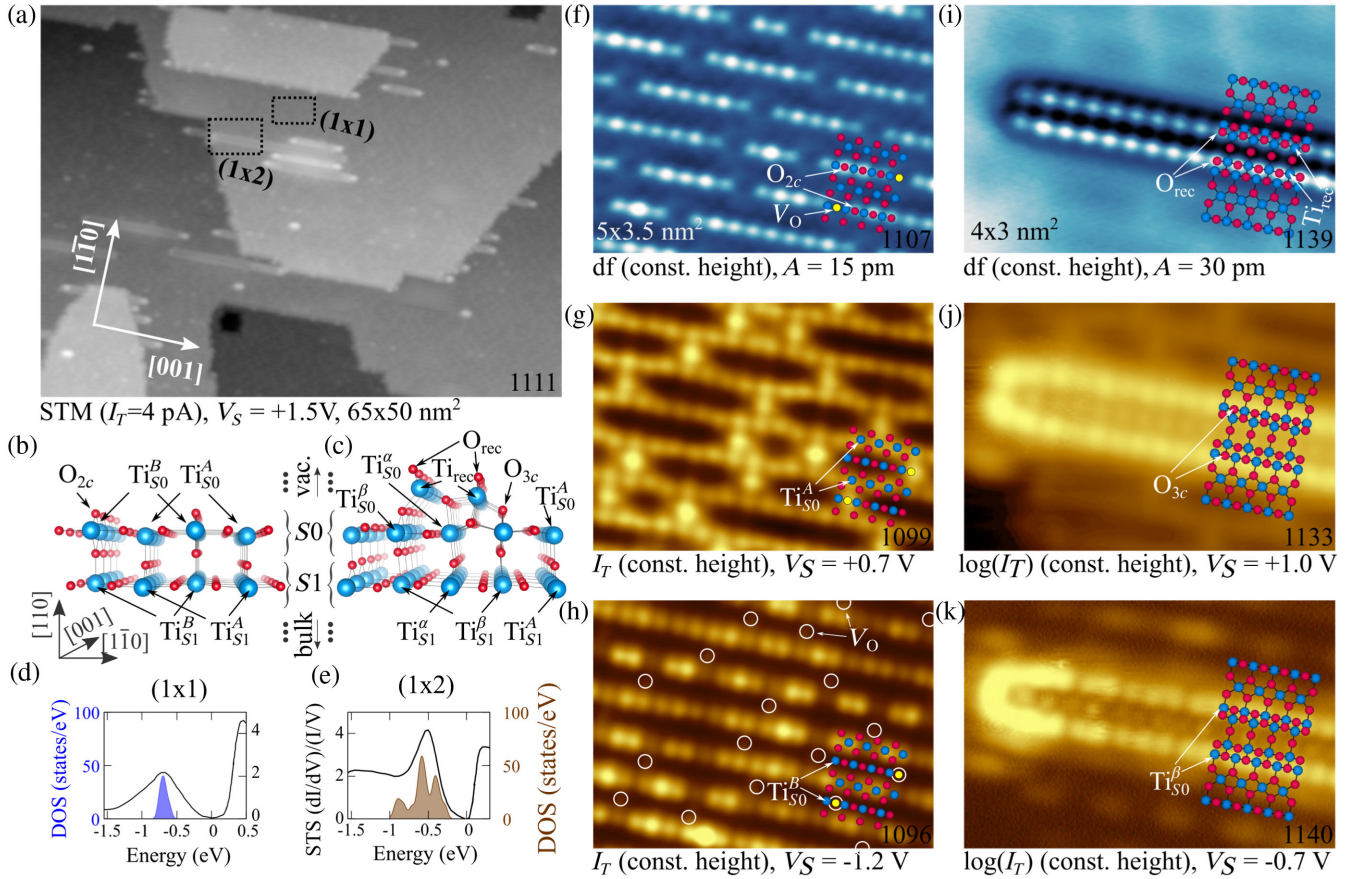

FIG. 1. The (1 × 1) and (1 × 2) surface phases of TiO_2(110). (a) Large-area STM image of a reduced rutile (110) single crystal. Unreconstructed (1 × 1) regions with single oxygen vacancies V_O appear together with reconstructed (1 × 2) Ti_2O_3 stripes. (b,c) Structural models of the (1 × 1) and (1 × 2) phases, respectively. (d,e) STS spectra (line) taken above (1 × 1) and (1 × 2), together with calculated polaronic gap states (filled area), shifted upwards by ≈0.25 eV to align the center of mass of the Ti^{3+} (polaronic) peaks with the experiment (in this way, the DFT peak positions are also in better agreement with the calculated vertical excitation energy E_{EL} [46]). (f)–(k) High-resolution images of the (1 × 1) and (1 × 2) regions marked in panel (a), overlaid with the respective structural models. AFM images (i,f) show the highest O atoms (O_{2c} and O_{rec}) on the surface, and STM images show the empty (g,j) and filled (h,k) states.

images of the (1 × 1) phase [the imaging mode most-widely employed in the literature, Fig. 1(g)], the V_O's appear as bright spots between the surface Ti^A_{S0} atoms. More interesting, however, are filled-states STM images that collect the gap states seen in STS [Fig. 1(d)]; the image in Fig. 1(h) directly shows the distribution of trapped polarons originating from the V_O's, as is discussed below. The lattice of the (1 × 2) reconstruction is very flexible and subject to surface buckling; see the DFT ground-state structural model shown in Fig. 1(c). Both experiment and DFT find competing structures with different degrees of buckling (discussed in Ref. [36]). When the buckling is small, like in Figs. 1(i)–1(k), the STM signal comes from the O_{3c} [empty states, Fig. 1(j)] and $Ti^{\alpha,\beta}_{SO}$ [in-gap states, Fig. 1(k)] atoms, the latter is attributed to Ti^{3+} polaronic-like states originating from the deviation of the Ti_2O_3 reconstruction from the stoichiometric formula. Our DFT calculations show that the reconstructed Ti_2O_3 (1 × 2) surface hosts two polarons per (1 × 2) unit cell. Therefore, the number of polarons that form in this structure is in accordance with a nominal V_O concentration of 50% (i.e., one missing oxygen per unit cell). This value is also in agreement with the electronic structure results shown in Fig. 1(e): The significant jump in the off-stoichiometry from the (1 × 1) to (1 × 2) reconstruction, 16.7% to (locally) 50%, implies a high concentration of polarons and causes the broadening of the in-gap peak in the DOS and filled-states STS [51–53] of the reconstructed surface [compare Figs. 1(d) and 1(e)].

We now turn our attention to the distribution of polarons in the (1 × 1) structure. It is generally agreed that excess electrons originating from impurities (such as V_O's but also other defects, e.g., interstitial Ti atoms [54]) form polarons preferentially located in the subsurface Ti^A_{S1} [001] rows. These can easily hop to surface sites when thermally activated [17,24,55–58], while a polaron trapping deeper in the bulk is significantly less favorable energetically, comparable to delocalized electrons [59]. We followed the

hopping in FPMD calculations and increased the polaron density by considering slabs with increasing c_{V_O} from 5.6% to 50.0%. Indeed, we found that at any c_{V_O}, the polarons are mostly located in the topmost two layers, $S0$ and $S1$, as reported by the histogram bars in Fig. 2. This result does not depend on the thickness of the simulated slab, corroborating the conclusion that in the (1×1) phase excess electrons form near-surface polarons [17,24] and avoid the bulk states suggested in recent literature [60]. At the smallest concentration, $c_{V_O} = 5.6\%$, the polarons are located in the $S1$ layer 95% of the time and undergo inter- and intra-Ti^{A}_{S1} row hopping [histogram bar of Fig. 2(a)]. Hopping into surface sites is very rare, with polarons being trapped in $S0$ for 5% of the time only. With increasing c_{V_O} in the surface (S0) layer [histogram bars of Figs. 2(b)–2(d)], i.e., with an increasing number of polarons in the system, hopping into $S0$ sites becomes more likely.

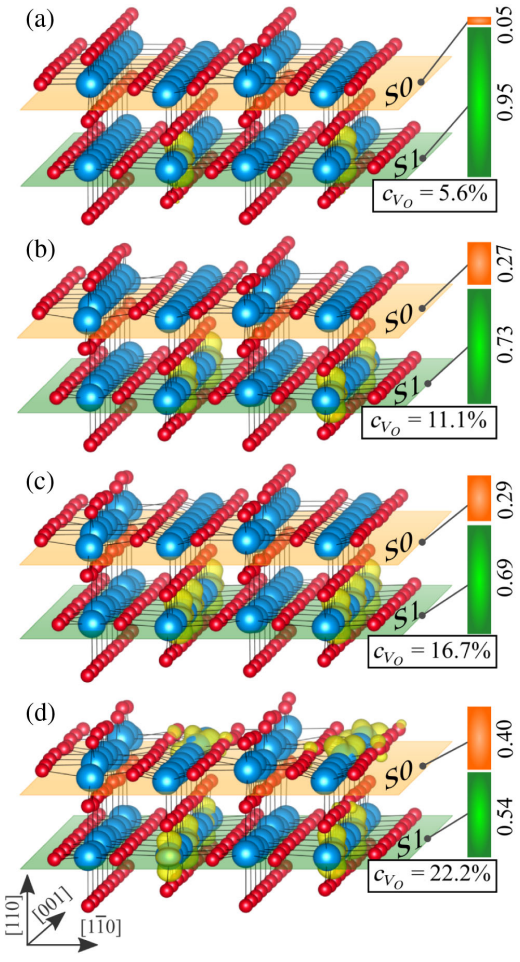

FIG. 2. Polaron distribution in $TiO_2(110)$. (a)–(d), Most stable polaron configurations obtained by FPMD and subsequent relaxations at the various V_O concentrations specified in each panel. The histograms illustrate how often the polarons are found in $S0$ (orange) and $S1$ (green) Ti sites during the FPMD runs.

Figure 2 also presents the charge density isosurfaces of polarons in their energetically most favorable configuration for each c_{V_O}. The stable configurations at low V_O concentration ($c_{V_O} \leq 16.7\%$) are characterized by polarons trapped only in $S1$ sites [Figs. 2(a)–2(c)]. At higher concentrations ($c_{V_O} \geq 22.2\%$), it is energetically more favorable to also host polarons in $S0$ sites rather than increasing their density in the $S1$ layer [Fig. 2(d)]. Interestingly, this c_{V_O} value in the calculations agrees with the V_O concentration of 16.7%, where the (1×1) and (1×2) phases are found to coexist in our experiment. Thus, the limited capacity of the subsurface ($S1$) layer to accommodate the polarons appears to be the driving force behind forming the (1×2) reconstruction.

In order to explain this characteristic feature of the polaronic distribution as a function of the concentration of oxygen vacancies, we recall here that polarons are negatively charged quasiparticles. Therefore, their Coulomb-like repulsion should increase with decreasing polaron-polaron distance. Indeed, during the FPMD runs, the probability of finding two polarons at adjacent sites is very low at any c_{V_O}. This is seen in Figs. 3(c)–3(e), where we report the polaron-polaron autocorrelation functions along the Ti^{A}_{S1} [001] rows. The highest probability is found for values that maximize the distance between polarons in the row, corresponding to three or four lattice constants apart, depending on the V_O density [Figs. 3(c)–3(e)]. This result is in excellent agreement with experiment, in particular, at $c_{V_O} = 16.7\%$ where a clear (3×1) periodicity is observed in the autocorrelation analysis of filled-states STM images [Fig. 3(g)]. We notice that, at larger V_O concentration ($c_{VO} \geq 22.2\%$), the peak of the calculated correlation function is not shifted to smaller distances, although the polaron density in the cell increases: The (3×1) pattern in $S1$ is preserved [Fig. 3(e)], and polarons populate the $S0$ layer more often [histogram bar of Fig. 2(d)]. This can be understood by inspecting the spatial extension of the polaron charge density. While most of the polaron charge has d_{z^2} symmetry [see inner yellow isosurface in Fig. 3(b)], a non-negligible amount of charge spreads across the adjacent Ti^{A}_{S0} and Ti^{A}_{S1} sites [see external isosurface in Fig. 3(b)]. This extended cloud gives rise to the STM contrast observed in experiment [Fig. 3(f)]—a characteristic dimerlike shape [Fig. 3(a)]—and clarifies the correlation between the distribution of polarons in $S1$ and the STM spots. The 3×1 periodicity of polarons along the Ti^{A}_{S1} row [sketched in Fig. 3(h)] avoids the overlap of two adjacent extended repulsive polaron clouds [Fig. 3(b)], thereby reducing the polaron-polaron repulsion, as recently confirmed in the literature [60]. In the FPMD runs at higher V_O concentrations, polarons are pushed into $S0$ sites in order to preserve the optimal concentration in the $S1$ layer. We also note that the polaron-polaron repulsion is perturbed by the attracting Coulomb interaction between polarons and the immobile V_O centers [16,61], which

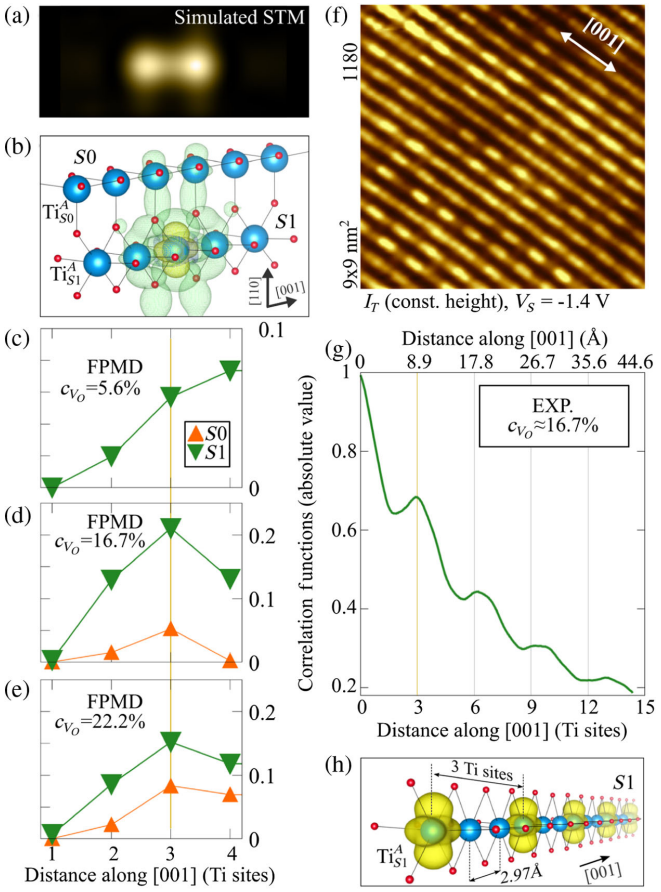

FIG. 3. Polaron distribution along the Ti^A_{S1} row. (a) Simulated filled-states STM (at 2 Å from the surface) of an isolated polaron around a Ti^A_{S1} site. (b) The corresponding charge density isosurface shows the high-density d_{z^2}-like orbital localized at Ti^A_{S1} (yellow) and the large, low-density cloud extending across the nearby Ti^A_{S1} and Ti^A_{S0} sites. (c)–(e) Calculated polaron-polaron autocorrelation functions along Ti^A_{S1} and Ti^A_{S0} rows extracted from FPMD runs at c_{V_O} = 5.6%, 16.7%, and 22.2%. (f) Experimental filled-states STM image at c_{V_O} = 16.7%, and (g) corresponding polaron-polaron autocorrelation function along the [001] rows. (h) Sketch of the 3 × 1 periodicity in the Ti^A_{S1} row.

modifies the optimum patterns, including the 3 × 1 (see Ref. [36] for more details).

The measured maximum V_O concentration of 16.7% on the (1 × 1) patches of the partially reconstructed surface suggests that a further increase in V_O results in a thermodynamically unstable situation, and this leads the system to the (1 × 2) reconstruction. This behavior is borne out of our *ab initio* calculations, but only if the polaron states are allowed to form [62]: We computed the surface free energy ΔG as a function of the oxygen chemical potential $\Delta\mu_O$ for each system [i.e., the (1 × 1) surface with c_{V_O} = 5.6%, 11.1%, 16.7%, 22.2%, 33.3%, 38.9%, 50.0% and the (1 × 2) reconstruction]. This computation was done both for the unrealistic case of excess electrons delocalized in the conduction band and for the polarons localized in their most favorable configuration. When polaron formation is included in the calculations, the phase diagram in Fig. 4(b) shows that the Ti_2O_3 reconstruction becomes the most stable one above the critical V_O concentration of 22.2%. This is slightly larger than the critical concentration measured experimentally, which could be attributable to effects not included in our calculations, such as the presence of additional dopants (e.g., interstitial Ti [54]), the V_O distribution, and the specific type of approximation (DFT + U) chosen to treat the localization effect [63]. Note, however, that the delocalized solution shown in Fig. 4(a) predicts that the reduced (1 × 1) phase remains the most stable structure even at high V_O concentrations: The Ti_2O_3 reconstruction [inset in Fig. 4(a)] is just as stable as the (1 × 1) at c_{V_O} = 50.0%.

IV. DISCUSSION

To understand this polaron-mediated change of the surface stability, it is instructive to analyze the energy gained upon polaron formation, E_{POL} [46]. It is defined as the total-energy difference between the polaronic and fully delocalized free-carrier solution, and it results from the competition between the strain energy required to distort the lattice, E_{ST}, and the electronic energy E_{EL} gained by localizing the electron at a Ti site in such a distorted lattice. Figure 5(a) shows E_{POL} for the most stable configuration at each considered c_{V_O}. For low concentrations, up to $c_{V_O} \simeq 20\%$ in the (1 × 1) structure, E_{POL} decreases with increasing concentration; it becomes more favorable to form polarons in the system. For $c_{V_O} > 22.2\%$, however, E_{POL} remains constant and ultimately increases. Figure 5(a) also includes the polaron energy for the reconstructed surface [64]. It has the highest negative value of all configurations considered, and the resulting convex hull clearly shows that the reduced (1 × 1) phases are unstable for $c_{V_O} > 22.2\%$. The surface undergoes a structural reconstruction above this critical value.

The trend of E_{POL} as a function of c_{V_O} becomes clear if one considers the energy cost that is required to locally distort the lattice in order to accommodate an electron and the energy gained by localizing an electron in such a lattice [46]. Figure 5(b) reports this strain energy E_{ST} for the most stable configuration at each considered c_{V_O}. E_{ST} decreases with increasing c_{V_O}, but it shows a distinct jump at the critical $c_{V_O} = 22.2\%$ [$\Delta E_{ST} = E_{ST}(22.2\%) - E_{ST}(16.7\%) = 65$ meV]. The isosurfaces plotted in Fig. 2 are helpful to understand this trend. At low concentrations, up to $c_{V_O} = 16.7\%$, the polarons reside preferentially along the Ti^A_{S1} [001] row. Once the lattice in the S1 layer is distorted (as well as the *S*0-*S*1 interlayer distance), it is increasingly easier to form more polarons. The *S*0 layer is kept essentially unperturbed. At c_{V_O} = 22.2%, however, the polarons also start to populate the S0 layer, and the breaking of the symmetry of the top layer

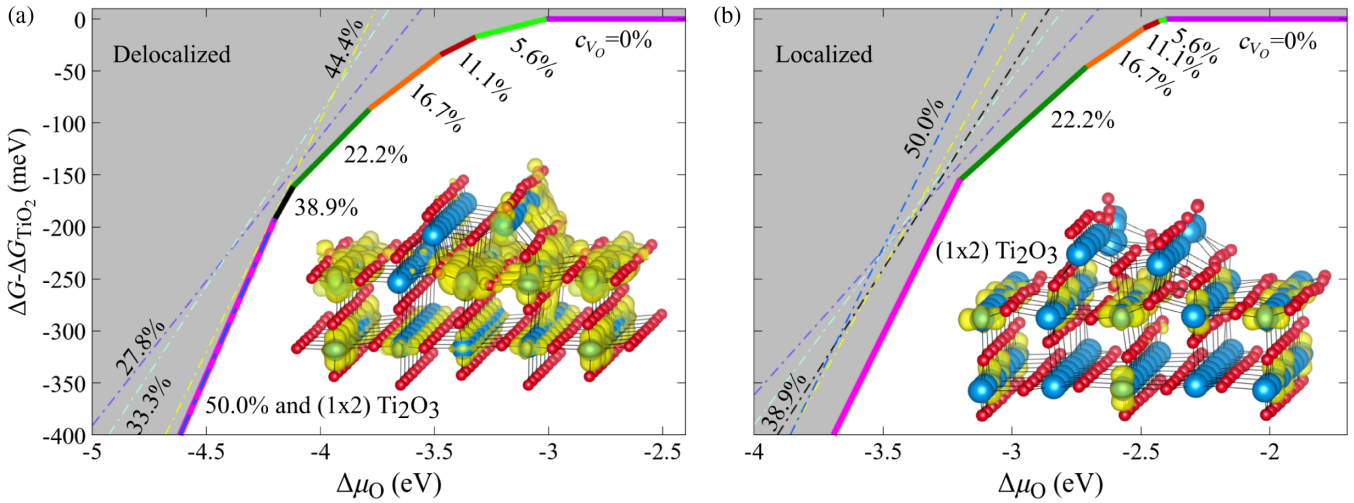

FIG. 4. $TiO_2(110)$ surface phase diagram. Surface free energy (ΔG) for the most stable configurations obtained from the MD for the reduced (1×1) structures at different V_O concentrations (all lines except pink) and for the (1×2) Ti_2O_3 reconstruction (pink line) as a function of the chemical potential $\Delta\mu_O$ with respect to the stoichiometric (1×1) phase. (a) Delocalized solution: Excess electrons are spread across all lattice sites and delocalized at the bottom of the conduction band. At $c_{V_O} = 50.0\%$, the (1×1) structure is degenerate with the (1×2) Ti_2O_3 reconstruction (Ti_2O_4 with 50% of V_O). (b) Localized solution: The excess electrons are trapped in distinct Ti sites, mostly located in $S0$. The insets show the distribution of excess electrons in the (1×2) structure. The localized polaron picture is capable of predicting the (1×1) to (1×2) transition, manifested by the increased stability of the reconstructed Ti_2O_3 phase at low oxygen chemical potential compared to the highly reduced (1×1) phases.

results in an additional energy cost. As pointed out above, increased jumping to $S0$ happens in order to preserve the optimum 3×1 pattern in $S1$ (reached at $c_{V_O} = 16.7\%$), as a larger polaron density in $S1$ would result in the overlap of the extended polaronic cloud, as well as in a strong Coulomb repulsion. While hosting polarons in both layers $S1$ and $S0$ reduces this overlap, it requires a distortion of the lattice around both the Ti^A_{S1} and Ti^A_{S0} sites. Apparently, a structural switch to a local (1×2) structure happens instead. The Ti_2O_3 reconstruction exhibits a high degree of structural flexibility, expressed in terms of a low energy cost E_{ST} [Fig. 5(b)] needed to accommodate a large concentration of polarons (i.e., as large as in the $c_{V_O} = 50\%$ case).

Finally, in Fig. 5(c), we show the evolution of E_{EL} as a function of c_{V_O}. First, we note that E_{EL} is about twice as larger as E_{ST}, and it leads to a large polaron energy at any V_O concentration. To understand the trend of E_{EL}, it is useful to correlate E_{EL} with the change in the polaron DOS with c_{V_O} [Figs. 1(d) and 1(e), and Fig. S9 in Ref. [36]). At low c_{V_O}, the polarons form a well-localized peak below the Fermi energy [Fig. 1(d)]. At $c_{V_O} = 22.2\%$, E_{EL} decreases by 100 meV because the additional polarons start to populate levels at lower energies (Fig. S9). For larger c_{V_O}, the peak exhibits a progressive broadening towards higher energies, which leads to an increase of E_{EL}.

The combined action of both the low strain cost E_{ST} and the favorable electronic localization energy E_{EL} determines the thermodynamic stability of the (1×2) phase, which overtakes the electrostatic instability from the trapped charges near the (1×1) surface. Moreover, the $Ti^{\alpha,\beta}_{S0}$ sites in the (1×2) reconstructed surface are easily reducible and can conveniently host polarons [see the advantageous formation energy E_{POL} in Fig. 5(a)]. The (1×2) phase is more stable than the highly reduced ($c_{V_O} = 50\%$) (1×1) surface by about $\Delta E_{POL} = 84$ meV ($\Delta E_{POL} = E^{1\times1}_{POL} - E^{1\times2}_{POL}$), and this energy gain arises predominantly from the difference in E_{EL} between the two phases, 64 meV [$\Delta E_{ST}(50\%) = 20$ meV].

A. Summary and conclusion

In conclusion, the present study shows that polarons (charges trapped at Ti lattice sites) play an important role for the stability of titania surfaces. At slightly reducing conditions, Ti^{3+} polarons are trapped in the subsurface sites of the (1×1) TiO_2 surface, with the optimal polaron-polaron distance being three lattice sites. As the polaron density increases, Ti^{3+} polarons are pushed to the less favorable Ti surface sites as well. This process, however, costs energy, so ultimately a transition to a (1×2) reconstruction with the formal stoichiometry of Ti_2O_3 occurs. If we neglect charge trapping and relaxation around the polaron, the reconstructed phase does not appear in the theoretical phase diagram.

Our results for the rutile TiO_2 (1×1) to (1×2) transition could present a new paradigm for surface reconstructions that involve trapped charges and the interaction among them. Polaron formation is ubiquitous

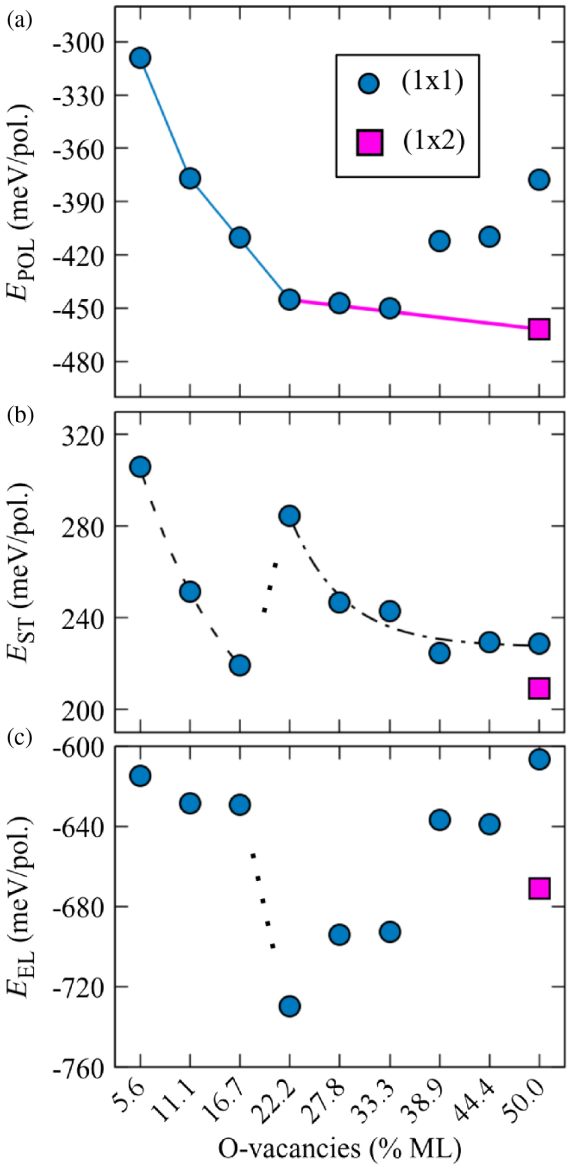

FIG. 5. Polaron energies (meV/polaron) as a function of c_{V_O}. (a) Polaron formation energy E_{POL}, computed as the difference between the ground states of the localized and delocalized solutions. (b) Strain energy E_{ST}, i.e., energy cost to locally distort the lattice in order to accommodate polarons. (c) Electronic energy E_{EL}, i.e., energy gained by localizing the electron in the distorted lattice.

in transition-metal oxides and is typically propelled by oxygen vacancies and doping [58]. Possible examples of other materials in which polaron-mediated reconstructions could be operational are oxide perovskites, in particular, $SrTiO_3$ [65–67], as well as popular oxides like ceria and hafnia [68]. Thus, this polaron-mediated mechanism is likely to be a pervasive phenomenon that could explain structural, electronic, and magnetic reconstructions at surfaces and interfaces [69] and could be employed to tune surface properties and to control the surface geometry. For instance, it is known that Nb-doped, V-doped, or Cr-doped TiO_2 samples form the (1×2) reconstruction much easier, even when the surrounding (1×1) phase has much lower V_O concentrations [70–72]. Finally, the control of charge trapping could provide a way to optimize the functionality of TiO_2-based memristors [73] and to facilitate charge transfer in catalytic processes [74].

ACKNOWLEDGMENTS

This work was supported by the Austrian Science Fund (FWF) SFB project VICOM (Grant No. F41), by the FWF project POLOX (Grant No. I 2460-N36), by the ERC Advanced Research Grant "OxideSurfaces," by the FWF Wittgenstein-prize (Z250-N16), and by the National Natural Science Foundation of China (Grants No. 21303156 and No. 21543006). The computational results presented have been achieved using the Vienna Scientific Cluster (VSC).

C. F., Ma. S., and U. D. conceived and coordinated the research project. M. R., C. F., P. F., and X. H. performed the DFT calculations. M. R. and P. F. conducted the statistical analysis. Ma. S. performed the experiments. Mi. S. and G. K. contributed to the data analysis. C. F., Ma.S., M. R., and U. D. wrote the manuscript. All authors contributed to the interpretation and discussion of the results.

[1] K. Oura, V. G. Lifshits, A. Saranin, A. V. Zotov, and M. Katayama, *Surface Science: An Introduction* (Springer-Verlag, Berlin, 2003).

[2] C. Noguera, *Polar Oxide Surfaces*, J. Phys. Condens. Matter **12**, R367 (2000).

[3] X.-Q. Wang, *Phases of the Au(100) Surface Reconstruction*, Phys. Rev. Lett. **67**, 3547 (1991).

[4] H. Onishi and Y. Iwasawa, *Reconstruction of* $TiO_2(110)$ *Surface: STM Study with Atomic-Scale Resolution*, Surf. Sci. **313**, L783 (1994).

[5] G. Binnig, H. Rohrer, C. Gerber, and E. Weibel, 7×7 *Reconstruction on Si(111) Resolved in Real Space*, Phys. Rev. Lett. **50**, 120 (1983).

[6] K. D. Brommer, M. Needels, B. Larson, and J. D. Joannopoulos, *Ab initio Theory of the* $Si(111)$-(7×7) *Surface Reconstruction: A Challenge for Massively Parallel Computation*, Phys. Rev. Lett. **68**, 1355 (1992).

[7] J. A. Enterkin, A. K. Subramanian, B. C. Russell, M. R. Castell, K. R. Poeppelmeier, and L. D. Marks, *A Homologous Series of Structures on the Surface of* $SrTiO_3(110)$, Nat. Mater. **9**, 245 (2010).

[8] Z. Wang, A. Loon, A. Subramanian, S. Gerhold, E. McDermott, J. A. Enterkin, M. Hieckel, B. C. Russell, R. J. Green, A. Moewes *et al.*, *Transition from Reconstruction Toward Thin Film on the (110) Surface of Strontium Titanate*, Nano Lett. **16**, 2407 (2016).

[9] W. Moritz and D. Wolf, *Structure Determination of the Reconstructed Au(110) Surface*, Surf. Sci. **88**, L29 (1979).

[10] K. M. Ho and K. P. Bohnen, *Stability of the Missing-Row Reconstruction on fcc (110) Transition-Metal Surfaces*, Phys. Rev. Lett. **59**, 1833 (1987).

[11] P. Heilmann, K. Heinz, and K. Mller, *The Superstructures of the Clean Pt(100) and Ir(100) Surfaces*, Surf. Sci. **83**, 487 (1979).

[12] G. Profeta and E. Tosatti, *Triangular Mott-Hubbard Insulator Phases of* Sn/Si(111) *and* Sn/Ge(111) *Surfaces*, Phys. Rev. Lett. **98**, 086401 (2007).

[13] H. Fröhlich, *Electrons in Lattice Fields*, Adv. Phys. **3**, 325 (1954).

[14] A. S. Alexandrov and J. T. Devreese, *Advances in Polaron Physics* (Springer-Verlag, New York, 2010).

[15] A. L. Shluger and A. M. Stoneham, *Small Polarons in Real Crystals: Concepts and Problems*, J. Phys. Condens. Matter **5**, 3049 (1993).

[16] P. Deák, B. Aradi, and T. Frauenheim, *Quantitative Theory of the Oxygen Vacancy and Carrier Self-Trapping in Bulk* TiO_2, Phys. Rev. B **86**, 195206 (2012).

[17] M. Setvin, C. Franchini, X. Hao, M. Schmid, A. Janotti, M. Kaltak, C. G. Van de Walle, G. Kresse, and U. Diebold, *Direct View at Excess Electrons in* TiO_2 *Rutile and Anatase*, Phys. Rev. Lett. **113**, 086402 (2014).

[18] E. Salje, A. S. Alexandrov, and W. Y. Liang, *Polarons and Bipolarons in High-Tc Superconductors and Related Materials* (Cambridge University Press, Cambridge, England, 2005).

[19] J. M. De Teresa, M. R. Ibarra, P. A. Algarabel, C. Ritter, C. Marquina, J. Blasco, J. Garcia, A. del Moral, and Z. Arnold, *Evidence for Magnetic Polarons in the Magnetoresistive Perovskites*, Nature (London) **386**, 256 (1997).

[20] H. M. Rønnow, C. Renner, G. Aeppli, T. Kimura, and Y. Tokura, *Polarons and Confinement of Electronic Motion to Two Dimensions in a Layered Manganite*, Nature (London) **440**, 1025 (2006).

[21] M. Wang, C. Bi, L. Li, S. Long, Q. Liu, H. Lv, N. Lu, P. Sun, and M. Liu, *Thermoelectric Seebeck Effect in Oxide-Based Resistive Switching Memory*, Nat. Commun. **5**, 4598 (2014).

[22] A. L. Linsebigler, G. Lu, and J. T. Yates, *Photocatalysis on* TiO_2 *Surfaces: Principles, Mechanisms, and Selected Results*, Chem. Rev. **95**, 735 (1995).

[23] N. A. Deskins, R. Rousseau, and M. Dupuis, *Localized Electronic States from Surface Hydroxyls and Polarons in* $TiO_2(110)$, J. Phys. Chem. C **113**, 14583 (2009).

[24] P. M. Kowalski, M. Farnesi Camellone, N. N. Nair, B. Meyer, and D. Marx, *Charge Localization Dynamics Induced by Oxygen Vacancies on the* $TiO_2(110)$ *Surface*, Phys. Rev. Lett. **105**, 146405 (2010).

[25] N. A. Deskins, R. Rousseau, and M. Dupuis, *Distribution of* Ti^{3+} *Surface Sites in Reduced* TiO_2, J. Phys. Chem. C **115**, 7562 (2011).

[26] U. Diebold, *The Surface Science of Titanium Dioxide*, Surf. Sci. Rep. **48**, 53 (2003).

[27] C. Di Valentin, G. Pacchioni, and A. Selloni, *Reduced and N-Type Doped* TiO_2*: Nature of* Ti^{3+} *Species*, J. Phys. Chem. C **113**, 20543 (2009).

[28] M. Li, W. Hebenstreit, L. Gross, U. Diebold, M. A. Henderson, D. R. Jennison, P. A. Schultz, and M. P. Sears, *Oxygen-Induced Restructuring of the* $TiO_2(110)$ *Surface: A Comprehensive Study*, Surf. Sci. **437**, 173 (1999).

[29] M. Li, W. Hebenstreit, and U. Diebold, *Morphology Change of Oxygen-Restructured* $TiO_2(110)$ *Surfaces by UHV Annealing: Formation of a Low-Temperature* (1×2) *Structure*, Phys. Rev. B **61**, 4926 (2000).

[30] K. F. McCarty and N. C. Bartelt, *The* $1 \times 1/1 \times 2$ *Phase Transition of the* $TiO_2(110)$ *Surface-Variation of Transition Temperature with Crystal Composition*, Surf. Sci. **527**, L203 (2003).

[31] K. F. McCarty and N. C. Bartelt, *Role of Bulk Thermal Defects in the Reconstruction Dynamics of the* $TiO_2(110)$ *Surface*, Phys. Rev. Lett. **90**, 046104 (2003).

[32] G. Kresse and J. Hafner, *Ab Initio Molecular Dynamics for Liquid Metals*, Phys. Rev. B **47**, 558 (1993).

[33] G. Kresse and J. Furthmüller, *Efficient Iterative Schemes for Ab Initio Total-Energy Calculations Using a Plane-Wave Basis Set*, Phys. Rev. B **54**, 11169 (1996).

[34] J. P. Perdew, K. Burke, and M. Ernzerhof, *Generalized Gradient Approximation Made Simple*, Phys. Rev. Lett. **77**, 3865 (1996).

[35] F. Aryasetiawan, K. Karlsson, O. Jepsen, and U. Schönberger, *Calculations of Hubbard U from First-Principles*, Phys. Rev. B **74**, 125106 (2006).

[36] See Supplemental Material at http://link.aps.org/supplemental/10.1103/PhysRevX.7.031053 for further details.

[37] Q. Wang, A. R. Oganov, Q. Zhu, and X.-F. Zhou, *New Reconstructions of the (110) Surface of Rutile* TiO_2 *Predicted by an Evolutionary Method*, Phys. Rev. Lett. **113**, 266101 (2014).

[38] I. Mochizuki, H. Ariga, Y. Fukaya, K. Wada, M. Maekawa, A. Kawasuso, T. Shidara, K. Asakura, and T. Hyodo, *Structure Determination of the Rutile-*$TiO_2(110)$*-*(1×2) *Surface Using Total-Reflection High-Energy Positron Diffraction (TRHEPD)*, Phys. Chem. Chem. Phys. **18**, 7085 (2016).

[39] J. Tersoff and D. R. Hamann, *Theory of the Scanning Tunneling Microscope*, Phys. Rev. B **31**, 805 (1985).

[40] K. Reuter and M. Scheffler, *Composition, Structure, and Stability of* $RuO_2(110)$ *as a Function of Oxygen Pressure*, Phys. Rev. B **65**, 035406 (2001).

[41] Z. Majzik, M. Setvín, A. Bettac, A. Feltz, V. Cháb, and P. Jelnek, *Simultaneous Current, Force and Dissipation Measurements on the Si(111)* 7×7 *Surface with an Optimized qPlus AFM/STM Technique*, Beilstein J. Nanotechnol. **3**, 249 (2012).

[42] M. Setvín, J. Javorský, D. Turčinková, I. Matolínová, P. Sobotík, P. Kocán, and I. Ošťádal, *Ultrasharp Tungsten Tips—Characterization and Nondestructive Cleaning*, Ultramicroscopy **113**, 152 (2012).

[43] A. Yurtsever, D. Fernandez-Torre, C. Gonzalez, P. Jelinek, P. Pou, Y. Sugimoto, M. Abe, R. Perez, and S. Morita, *NC-AFM Imaging of the* $TiO_2(110)$*-*(1×1) *Surface at Low Temperature*, Phys. Rev. B **85**, 125416 (2012).

[44] R. Bechstein, C. González, J. Schütte, P. Jelínek, R. Pérez, and A. Kühnle, *All-Inclusive Imaging of the Rutile* $TiO_2(110)$ *Surface Using NC-AFM*, Nanotechnology **20**, 505703 (2009).

[45] L. Gross, F. Mohn, N. Moll, P. Liljeroth, and G. Meyer, *The Chemical Structure of a Molecule Resolved by Atomic Force Microscopy*, Science **325**, 1110 (2009).

[46] A. Janotti, C. Franchini, J. B. Varley, G. Kresse, and C. G. Van de Walle, *Dual Behavior of Excess Electrons in Rutile* TiO_2, Phys. Status Solidi RRL **7**, 199 (2013).

[47] C. L. Pang, S. A. Haycock, H. Raza, P. W. Murray, G. Thornton, O. Gülseren, R. James, and D. W. Bullett, *Added Row Model of* $TiO_2(110)1 \times 2$, Phys. Rev. B **58**, 1586 (1998).

[48] K. T. Park, M. Pan, V. Meunier, and E. W. Plummer, *Reoxidation of* $TiO_2(110)$ *via Ti Interstitials and Line Defects*, Phys. Rev. B **75**, 245415 (2007).

[49] N. Shibata, A. Goto, S.-Y. Choi, T. Mizoguchi, S. D. Findlay, T. Yamamoto, and Y. Ikuhara, *Direct Imaging of Reconstructed Atoms on* TiO_2 *(110) Surfaces*, Science **322**, 570 (2008).

[50] K.-O. Ng and D. Vanderbilt, *Structure and Apparent Topography of* $TiO_2(110)$ *Surfaces*, Phys. Rev. B **56**, 10544 (1997).

[51] M. Batzill, K. Katsiev, D. J. Gaspar, and U. Diebold, *Variations of the Local Electronic Surface Properties of* $TiO_2(110)$ *Induced by Intrinsic and Extrinsic Defects*, Phys. Rev. B **66**, 235401 (2002).

[52] C. Sànchez-Sànchez, M. G. Garnier, P. Aebi, M. Blanco-Rey, P. L. de Andres, J. A. Martín-Gago, and M. F. López, *Valence Band Electronic Structure Characterization of the Rutile* TiO_2 (110)-(1×2) *Reconstructed Surface*, Surf. Sci. **608**, 92 (2013).

[53] C. M. Yim, C. L. Pang, and G. F. Thornton, *Probing the Local Electronic Structure of the Cross-Linked* (1×2) *Reconstruction of Rutile* $TiO_2(110)$, Surf. Sci. **650**, 71 (2016), The Surface Science of Heterogeneous Catalysis: In Honor of Robert J. Madix.

[54] S. Wendt, P. T. Sprunger, E. Lira *et al.*, *The Role of Interstitial Sites in the Ti3d Defect State in the Band Gap of Titania*, Science **320**, 1755 (2008).

[55] S. Livraghi, S. Maurelli, M. C. Paganini, M. Chiesa, and E. Giamello, *Probing the Local Environment of* Ti^{3+} *Ions in* TiO_2 *(Rutile) by* ^{17}O *HYSCORE*, Angew. Chem., Int. Ed. **50**, 8038 (2011).

[56] V. E. Henrich, G. Dresselhaus, and H. J. Zeiger, *Observation of Two-Dimensional Phases Associated with Defect States on the Surface of* TiO_2, Phys. Rev. Lett. **36**, 1335 (1976).

[57] A. C. Papageorgiou, N. S. Beglitis, C. L. Pang, G. Teobaldi, G. Cabailh, Q. Chen, A. J. Fisher, W. A. Hofer, and G. Thornton, *Electron Traps and Their Effect on the Surface Chemistry of* $TiO_2(110)$, Proc. Natl. Acad. Sci. U.S.A. **107**, 2391 (2010).

[58] P. G. Moses, A. Janotti, C. Franchini, G. Kresse, and C. G. Van de Walle, *Donor Defects and Small Polarons on the* $TiO_2(110)$ *Surface*, J. Appl. Phys. **119**, 181503 (2016).

[59] S. Yang, A. T. Brant, N. C. Giles, and L. E. Halliburton, *Intrinsic Small Polarons in Rutile* TiO_2, Phys. Rev. B **87**, 125201 (2013).

[60] T. Shibuya, K. Yasuoka, S. Mirbt, and B. Sanyal, *Subsurface Polaron Concentration as a Factor in the Chemistry of Reduced* TiO_2 *(110) Surfaces*, J. Phys. Chem. C **121**, 11325 (2017).

[61] P. Deák, B. Aradi, and T. Frauenheim, *Oxygen Deficiency in* TiO_2*: Similarities and Differences Between the Ti Self-Interstitial and the O Vacancy in Bulk Rutile and Anatase*, Phys. Rev. B **92**, 045204 (2015).

[62] X. Hao, Z. Wang, M. Schmid, U. Diebold, and C. Franchini, *Coexistence of Trapped and Free Excess Electrons in* $SrTiO_3$, Phys. Rev. B **91**, 085204 (2015).

[63] T. Shibuya, K. Yasuoka, S. Mirbt, and B. Sanyal, *A Systematic Study of Polarons Due to Oxygen Vacancy Formation at the Rutile* $TiO_2(110)$ *Surface by* $GGA + U$ *and HSE06 Methods*, J. Phys. Condens. Matter **24**, 435504 (2012).

[64] For the (1×2) phase, we also call localization energy E_{POL} for simplicity, though the underlying physics of localization may also involve effects other than polaronic distortions.

[65] Z. Wang, A. Loon, A. Subramanian, S. Gerhold, E. McDermott, J. A. Enterkin, M. Hieckel, B. C. Russell, R. J. Green, A. Moewes *et al.*, *Transition from Reconstruction Toward Thin Film on the (110) Surface of Strontium Titanate*, Nano Lett. **16**, 2407 (2016).

[66] N. Erdman, K. R. Poeppelmeier, M. Asta, O. Warschkow, D. E. Ellis, and L. D. Marks, *The Structure and Chemistry of the* TiO_2*-Rich Surface of* $SrTiO_3(001)$, Nature (London) **419**, 55 (2002).

[67] X. Hao, Z. Wang, M. Schmid, U. Diebold, and C. Franchini, *Coexistence of Trapped and Free Excess Electrons in* $SrTiO_3$, Phys. Rev. B **91**, 085204 (2015).

[68] A. M. Stoneham, J. Gavartin, A. L. Shluger, A. V. Kimmel, D. Muoz Ramo, H. M. Rnnow, G. Aeppli, and C. Renner, *Trapping, Self-Trapping and the Polaron Family*, J. Phys. Condens. Matter **19**, 255208 (2007).

[69] C. Cancellieri, A. S. Mishchenko, U. Aschauer, A. Filippetti, C. Faber, O. S. Barisic, V. A. Rogalev, T. Schmitt, N. Nagaosa, and V. N. Strocov, *Polaronic Metal State at the* $LaAlO_3/SrTiO_3$ *Interface*, Nat. Commun. **7**, 10386 (2016).

[70] R. Shimizu, K. Iwaya, T. Ohsawa, T. Hasegawa, T. Hashizume, and T. Hitosugi, *Simplified Method to Prepare Atomically-Ordered* $TiO_2(110)$-(1×1) *Surfaces with Steps and Terraces*, Appl. Surf. Sci. **257**, 4867 (2011).

[71] X. Song, E. Primorac, H. Kughlenbeck, and H.-J. Freund, *Effect of Vanadium Admixing on the Surface Structure of* TiO_2 *(110) under Non-oxidizing Conditions*, Surf. Sci. **653**, 181 (2016).

[72] R. Bechstein, M. Kitta, J. Schutte, A. Kuhnle, and H. Onishi, *Evidence for Vacancy Creation by Chromium Doping of Rutile Titanium Dioxide (110)*, J. Phys. Chem. C **113**, 3277 (2009).

[73] E. Gale, TiO_2*-Based Memristors and ReRAM: Materials, Mechanisms and Models (A Review)*, Semicond. Sci. Technol. **29**, 104004 (2014).

[74] M. A. Henderson, *A Surface Science Perspective on Photocatalysis*, Surf. Sci. Rep. **66**, 185 (2011).